Journal of Materials Chemistry A

ROYAL SOCIETY OF CHEMISTRY

PAPER

View Article Online
View Journal

Check for updates

Cite this: DOI: 10.1039/d5ta08719h

Anchoring electron-delocalized CeO_2 on porous carbon for expediting polysulfide kinetics toward high-loading Li–S batteries

Zhe Yang,†[a] Shenglin Liu,†[c] Kai Chen,[b] Guodong Zhang,*[b] Feng Gong,*[c] Shuangxi Xing*[a] and Jian Wang*[de]

Received 27th October 2025
Accepted 30th November 2025

DOI: 10.1039/d5ta08719h

rsc.li/materials-a

High-energy-density lithium sulfur batteries with high mass loading are restricted by the depressive electrochemical kinetics of polysulfide conversion. Herein, to enhance catalytic efficiency, abundant electron-delocalized CeO_2 nanoparticles are anchored on the surface of pollen-derived carbon (PC-CeO_2) *via* one-step carbonization, serving as a sulfur host. In this design, pollen-derived carbon (PC) with a porous structural network enhances the electrical conductivity of the sulfur cathode while alleviating volume expansion and maintaining the stability of the cathode. The strategic incorporation of electron-delocalized CeO_2 nanoparticles is beneficial for the adsorption and catalysis of polysulfides, limiting the shuttle effect of polysulfides and effectively facilitating the electrochemical conversion kinetics. As a result, the fabricated sulfur cathode (PC-CeO_2/S) exhibits excellent electrochemical stability with a decay rate per cycle of 0.054% after 1000 cycles at 1C and outstanding rate performance (703.3 mAh g^{-1} at 3C). Furthermore, it achieves an impressive areal capacity of 5.64 mAh cm^{-2} at 0.2C even with a high sulfur loading of 5.5 mg cm^{-2}, demonstrating its potential for practical, high-energy-density applications in lithium–sulfur batteries.

Open Access Article. Published on 01 December 2025. Downloaded on 1/22/2026 2:28:10 AM.
This article is licensed under a Creative Commons Attribution 3.0 Unported Licence.

1. Introduction

Lithium–sulfur batteries are considered as the next-generation energy storage system owing to their excellent theoretical specific capacity (1675 mAh g^{-1}) and energy density (2600 Wh kg^{-1}).[1–3] However, the poor conductivity of sulfur and its discharge products (Li_2S/Li_2S_2) results in a decline in sulfur utilization, and the volume expansion in the sulfur cathode also undermines the stability of the electrode structure.[4–6] Besides, the shuttling effect and slow redox kinetic process of Li polysulfides (LiPSs) present substantial barriers to their application in lithium–sulfur batteries.[7–9] Therefore, introducing host materials to modify sulfur cathodes is an efficient strategy to realize further development in lithium–sulfur batteries.[10,11]

Researchers have made many attempts to design and synthesize advanced sulfur host materials to solve the above problems in the sulfur cathode.[12–15] Carbon materials, including carbon nanotubes, graphene and conductive carbon black, are widely used as sulfur host materials[16,17] because of their high electronic conductivity, good compatibility with sulfur and excellent chemical stability.[18–20] Nevertheless, non-polar carbon materials find it difficult to inhibit the shuttle effect effectively because of their weak interactions with LiPSs, ultimately leading to severe capacity decay.[21–23] The strategic doping modification of carbon-based materials is a useful approach for improving the adsorption capacity. For example, the incorporation of non-metallic heteroatoms, such as N and O, into the carbon matrix not only enhances its intrinsic electronic conductivity but also significantly increases its polarity, greatly improving its adsorption capacity and mitigating the shuttle effect.[24–27] Furthermore, researchers have frequently integrated polar metal compounds with carbon-based frameworks to obtain advanced composite materials, aiming to synergistically enhance the chemical adsorption and catalytic ability of LiPSs.[28–30] This strategic modification improves the conductivity of carbon while introducing strong polar interactions that effectively adsorb and inhibit LiPSs. Simultaneously, the catalytic activity of these metal compounds accelerates the redox kinetics of LiPS conversion, which mitigates the sluggish reaction rates and suppresses the shuttle effect, thereby optimizing

[a]Faculty of Chemistry, Northeast Normal University, Changchun 130024, P. R. China. E-mail: xingsx737@nenu.edu.cn

[b]Department of Physics, Research Institute for Biomimetics and Soft Matter, Fujian Provincial Key Laboratory for Soft Functional Materials, Xiamen University, Xiamen 361005, P. R. China. E-mail: zhanggd710@nenu.edu.cn

[c]Key Laboratory of Energy Thermal Conversion and Control of Ministry of Education, School of Energy and Environment, Southeast University, Nanjing, 211189, Jiangsu, China. E-mail: gongfeng@seu.edu.cn

[d]Karlsruhe Institute of Technology (KIT), D76021 Karlsruhe, Germany. E-mail: jian.wang@kit.edu; wangjian2014@sinano.ac.cn

[e]Helmholtz Institute Ulm (HIU)D89081 Ulm, Germany

† These authors contributed equally to this work.

Open Access Article. Published on 01 December 2025. Downloaded on 1/22/2026 2:28:10 AM. This article is licensed under a Creative Commons Attribution 3.0 Unported Licence.

the overall electrochemical performance of lithium–sulfur batteries.[31–34]

As a carbon precursor, pollen-derived carbon has the following advantages: (1) intrinsic elemental composition of pollen: owing to its richness in various non-metallic elements, PC undergoes direct *in situ* modification during carbonization, which produces a conductive and polar carbon matrix without additional doping steps. (2) Hierarchical porosity and structural stability: the naturally self-organized porous network of pollen-derived carbon facilitates efficient sulfur loading while simultaneously alleviating the volumetric expansion of sulfur during lithiation and maintaining structural stability. (3) Sustainable and green chemistry approach: as an abundant and renewable biomass material, PC avoids special and complex synthesis routes, reflecting the advantages of green chemistry.[35,36] In order to further improve the adsorption and catalytic performance of carbon materials, the incorporation of metallic compounds is often necessary to form an active interface. Among the available materials, cerium dioxide (CeO_2) has received significant attention due to its extraordinary properties:[14,37,38] (1) CeO_2 possesses a unique Ce^{3+}/Ce^{4+} redox couple, which actively participates in accelerating the reversible catalytic conversion of LiPSs. (2) Abundant oxygen vacancies in CeO_2 serve as active sites to enhance the chemisorption and catalytic conversion of LiPSs.

In this study, to enhance catalytic efficiency, abundant electron-delocalized CeO_2 nanoparticles anchored on the surface of pollen-derived carbon materials (PC-CeO_2) are prepared through a carbonization process. The obtained PC-CeO_2 reduced the volume expansion, which maintained the stability and integrity of the structure due to its special and robust structure. Meanwhile, it provided sufficient active sites of electron delocalization for the chemical adsorption and catalytic kinetic conversion of LiPSs. DFT theoretical calculations further prove the strong adsorption and catalytic capacity of PC-CeO_2 towards sulfur species. As a result, the PC-CeO_2/S cathode demonstrated outstanding electrochemical performance with a low fading rate of 0.054% per cycle at 1C after 1000 cycles and an outstanding rate capacity of 703.3 mAh g^{-1} at 3C. Even with a high sulfur loading of 5.5 mg cm^{-2}, the PC-CeO_2/S electrode exhibited a high capacity of 5.64 mAh cm^{-2} at 0.2C after 60 cycles, which reached commercial standards of 4.0 mAh cm^{-2}.

2. Results and discussion

The synthesis and preparation process of pollen-derived porous carbon anchored with CeO_2 NPs are illustrated in Fig. 1a. Initially, the pollen is treated with water and acetone to remove fats, sugars and other substances. Then, the as-synthesized CeO_2 NPs are anchored on the surface of the pollen-derived carbon upon high-temperature carbonization at 900 °C to achieve PC-CeO_2. The PC-CeO_2/S is further obtained after the sulfur loading treatment. As shown in the TEM image (Fig. 1b), the CeO_2 NPs display a highly uniform size distribution across the samples, which are uniformly distributed on the PC surface with a porous skeleton (Fig. 1c and S1a–c), The HRTEM image of PC-CeO_2 (Fig. 1d) distinctly reveals a lattice spacing of 0.31 nm, which corresponds to the (111) plane of CeO_2, verifying the structural integrity of the CeO_2 NPs within the composite.[39] Furthermore, the EDS elemental mapping images (Fig. 1e) demonstrate the uniform presence of Ce, O, C and N elements within PC-CeO_2. Besides, as shown in Fig. S2a and b, both the interior and surface of PC-CeO_2 and PC are filled with sulfur after sulfur fixation. In addition, compared with PC, the incorporation of CeO_2 NPs into PC results in a reduction in the specific surface area (9.56 m^2 g^{-1} for PC-CeO_2 *vs.* 20.60 m^2 g^{-1} for PC, as shown in Fig. S3a and b), which leads to the formation of a hybrid holey structure with an amount of mesopores (Fig. S4a and b). The above results verify the successful integration and structural modification of PC with CeO_2 NPs. After the sulfur is loaded, the specific surface areas of both PC-CeO_2 and PC decrease, as shown in Fig. S5a and b. Furthermore, PC-CeO_2/S exhibits obvious mesoporous pores in Fig. S5c, which contributes to the inhibition of the shuttle effect of LiPSs.

To further confirm the composition and structural characteristics of the material, the relevant characterization results are displayed in Fig. 1f–j. In the XRD patterns of PC-CeO_2 and CeO_2 (Fig. 1f), the diffraction peaks at 28.5°, 33.1°, 47.5° and 56.3° are attributed to the (111), (200), (220) and (311) planes of CeO_2 (PDF#34-0394), respectively, while the XRD pattern of PC shows two distinct carbon peaks.[40] To investigate the configuration of carbon in PC-CeO_2 and PC, the Raman spectrum was carried out, as shown in Fig. 1g. Two prominent peaks emerge at 1350 and 1580 cm^{-1}, corresponding to the D and G bands of the carbon layer, respectively. Besides, the intensity ratios (I_D/I_G) for PC-CeO_2 and PC are estimated to be 0.98 and 0.96, respectively. This marked difference underscores more defects exhibited by the PC-CeO_2 composite, which plays a pivotal role in optimizing the rapid transport of electron ions during electrochemical process, thereby improving the electrochemical performance. In addition, XPS measurements were carried out to determine the surface chemistry phase and composition of the PC-CeO_2 composite. The XPS full spectrum of PC-CeO_2 verifies the presence of Ce, O, N and C elements (Fig. S6a). As depicted in Fig. S6b, the C 1s spectrum displays four distinct peaks at 284.8 eV (C–C), 286.1 eV (C–N), 287.2 eV (C–O) and 289.2 eV (C=O). Fig. S6c shows three peaks, including pyridinic-N (398.4 eV), pyrrolic-N (400.7 eV) and graphitic-N (401.7 eV). As shown in Fig. 1h, the Ce 3d spectrum exhibits eight distinct splitting peaks. The peaks at 917.1, 908.2, 901.2, 898.6, 888.6, and 882.7 eV can be ascribed to Ce^{4+}, while others located at 904.1 and 885.7 eV belong to Ce^{3+}. In addition, the oxygen vacancy of PC-CeO_2 can be verified by O1s XPS (Fig. 1i). The peaks at 529.5 eV are connected to metal oxygen, and the peaks at 531.5 eV are attributed to a low-coordinated oxygen vacancy.[41] EPR is used to further estimate the oxygen vacancy of PC-CeO_2 (Fig. 1j). The representative EPR signal at $g = 2.002$ reveals electron capture at the oxygen vacancy.[42,43] The above results explain that the addition of CeO_2 NPs plays a pivotal role in promoting chemical adsorption and accelerating the catalytic conversion of LiPSs.[42,44] The sulfur contents in PC-CeO_2/S, CeO_2/S and PC/S are 75, 71.2 and 74.2 wt%, respectively (Fig. S7). Besides, the EDS elemental mapping of the PC-CeO_2/S in Fig. S8

 This journal is © The Royal Society of Chemistry 2025

Open Access Article. Published on 01 December 2025. Downloaded on 1/22/2026 2:28:10 AM.
This article is licensed under a Creative Commons Attribution 3.0 Unported Licence.

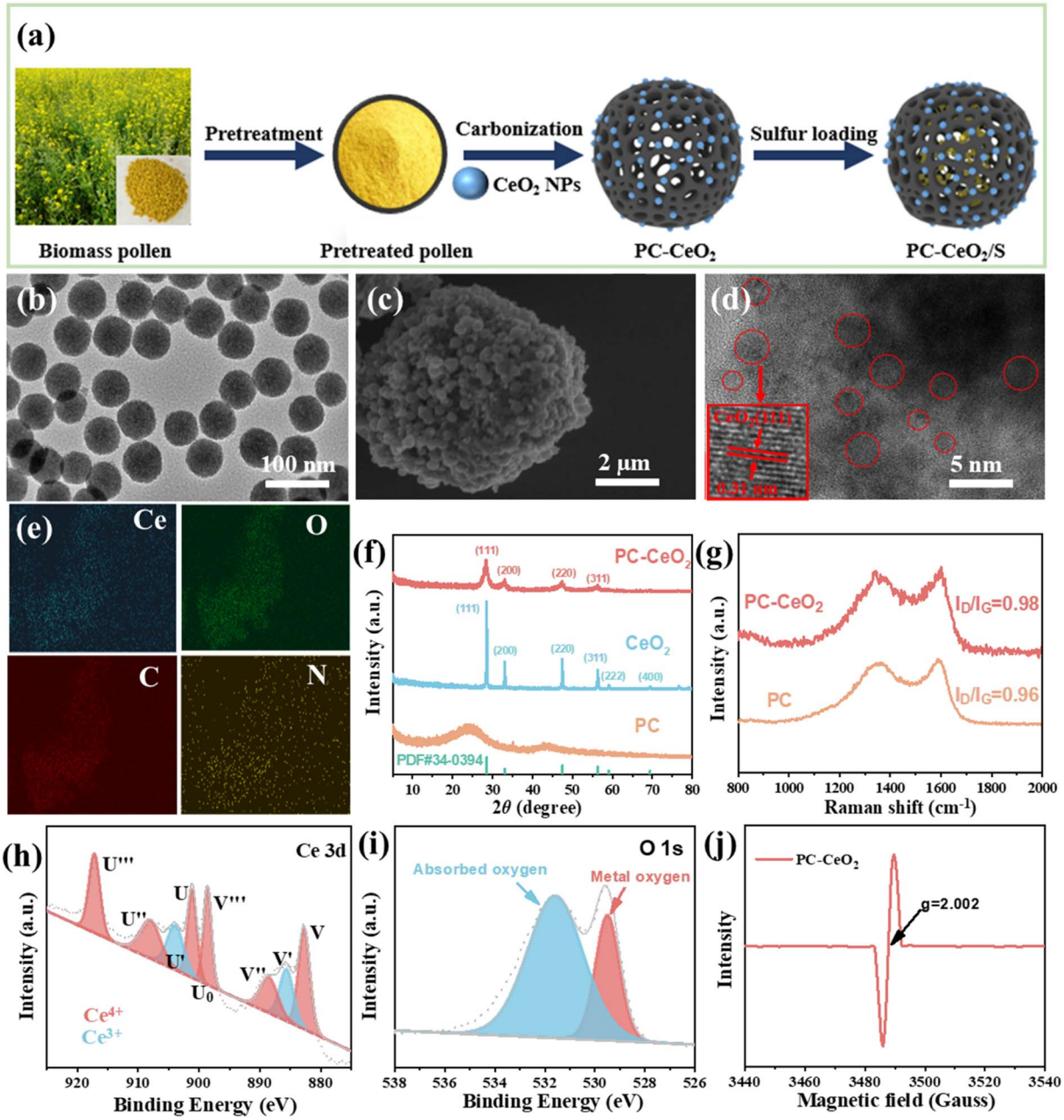

Fig. 1 (a) The preparation process of PC-CeO_2 and PC-CeO_2/S; (b) TEM image of the CeO_2 nanoparticles; (c) SEM image of PC-CeO_2; (d) HRTEM image of PC-CeO_2; (e) the corresponding elemental mapping images of Ce, O, C and N in PC-CeO_2; (f) XRD patterns of PC, CeO_2 and PC-CeO_2; (g) Raman spectra of PC and PC-CeO_2; (h) Ce 3d and (i) O 1s XPS spectra of PC-CeO_2; and (j) EPR curve of PC-CeO_2.

confirms the uniform distribution of sulfur. These findings demonstrate the remarkable sulfur-holding ability of the PC-CeO_2 composite.

To further demonstrate the adsorption capacity of different materials for LiPSs, visual adsorption experiments were carried out. As illustrated in Fig. 2a, the color in Li_2S_6 with PC-CeO_2 nearly vanishes after 2 h, and the UV-vis data further confirm its exceptional adsorption ability. Furthermore, XPS analysis of LiPS adsorption was performed to analyze the possible mechanism of the strong anchoring effect for LiPSs on PC-CeO_2, as shown in Fig. 2b and c. After exposure to Li_2S_6, the Ce 3d peaks exhibit an obvious shift toward lower binding energies, indicating that Ce cations actively participate in the redox interactions. This shift confirms the involvement of the Ce^{4+}/Ce^{3+} redox couple, highlighting their crucial role as electron transfer mediators during the Li_2S_6 adsorption process. As depicted in Fig. 2c, the peaks at 165.2 and 164.0 eV correspond to S_2^{2-}, and the signals at 168.4 and 169.4 eV correspond to SO_3^{2-} and SO_4^{2-} (thiosulfate), respectively.[44] All the above data indicate a strong interaction between PC-CeO_2 and Li_2S_6. Li_2S plays a crucial role in the reaction process of lithium–sulfur batteries, affecting the charge and discharge capacity of the batteries. Thus, nucleation

Open Access Article. Published on 01 December 2025. Downloaded on 1/22/2026 2:28:10 AM.
This article is licensed under a Creative Commons Attribution 3.0 Unported Licence.

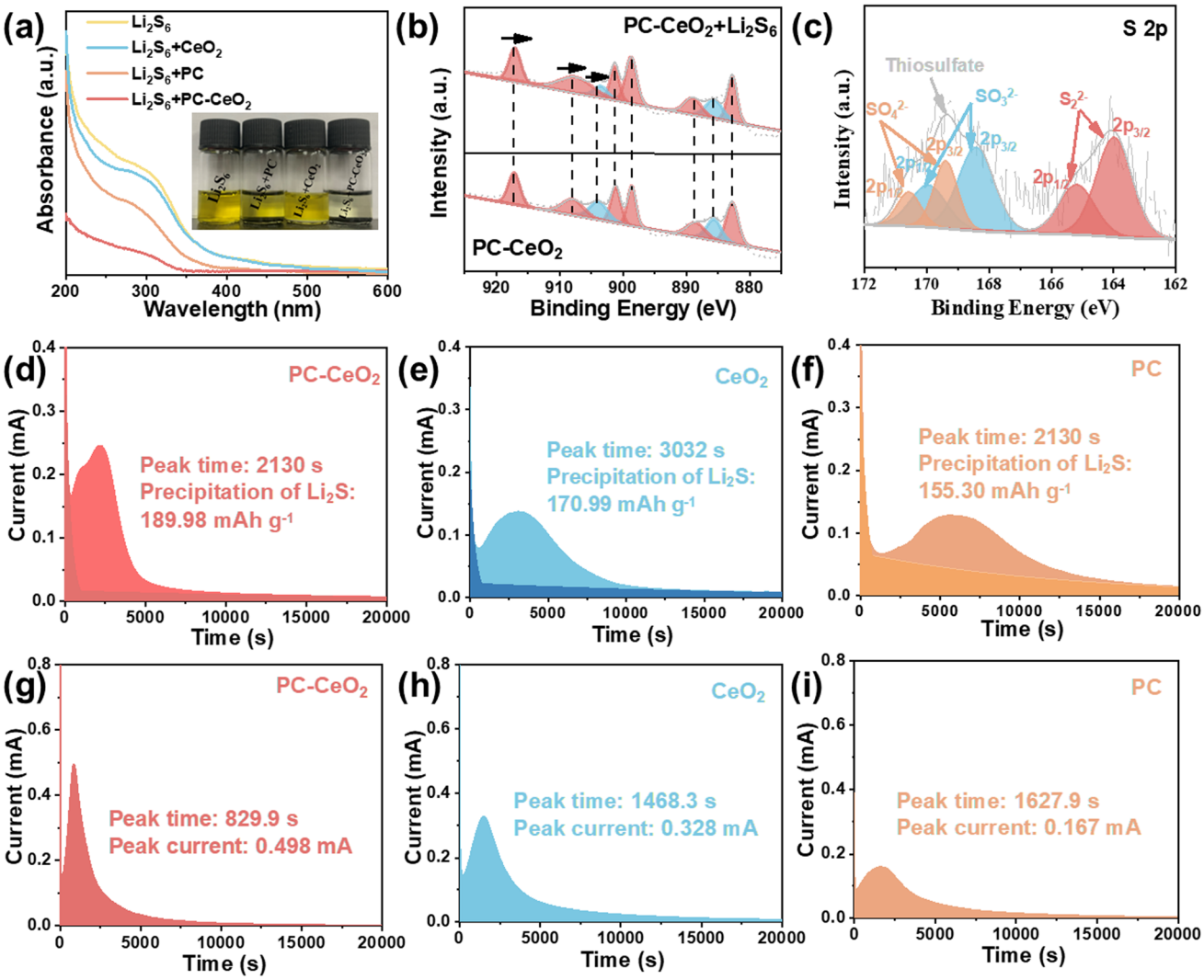

Fig. 2 (a) Visual adsorption tests of pure Li_2S_6 solutions, PC + Li_2S_6, CeO_2 + Li_2S_6 and PC-CeO_2 + Li_2S_6. (b) Ce 3d XPS spectra of PC-CeO_2 and PC-CeO_2 + Li_2S_6. (c) S 2p XPS spectra of PC-CeO_2 + Li_2S_6. Precipitation profiles of Li_2S with (d) PC-CeO_2, (e) CeO_2 and (f) PC. Dissolution profiles of Li_2S with (g) PC-CeO_2, (h) CeO_2 and (i) PC.

(Fig. 2d–f) and dissolution experiments of Li_2S (Fig. 2g–i) were carried out. The results indicate that the PC-CeO_2 electrode exhibits the earliest current peak at 2130 s and the largest deposition capacity at 189.98 mAh g^{-1}. Besides, as shown in Fig. 2g–i, the dissolution profiles of Li_2S display that the PC-CeO_2 electrode exhibits the earliest current response and largest current peak (829.9 s/0.498 mA). Therefore, PC-CeO_2 significantly enhances liquid–solid reactions and accelerates the conversion of LiPSs in Li–S batteries.

The cyclic voltammetry (CV) profiles for Li–S batteries equipped with PC-CeO_2, CeO_2 and PC electrodes are depicted in Fig. 3a. Two notable reduction peaks, labeled peaks A and B, appear around 2.30 V and 2.02 V, respectively. These correspond to the stepwise reduction process of S_8 to lithium polysulfides (Li_2S_n, $4 \leq n \leq 8$) and their subsequent transformation into shorter, insoluble species, like Li_2S_2 and Li_2S. The oxidation peak, denoted as peak C at 2.31 V, marks the reverse reaction, where Li_2S_2 and Li_2S are oxidized back to S_8. Among these, the PC-CeO_2 electrode stands out with the highest current response and the smallest reaction polarization (0.295 V for PC-CeO_2 *vs.* 0.314 V for CeO_2 and 0.358 V for PC), signifying its superior electrochemical performance in Li–S batteries. Fig. 3b and c illustrate the enlarged CV curve segments around peaks A and C in Fig. 3a. Tafel plots were derived based on these peaks, revealing that the PC-CeO_2 electrode exhibits lower Tafel slopes (27.3 mV dec^{-1} for peak A and 98.91 mV dec^{-1} for peak C) than the CeO_2 electrode (28.2 mV dec^{-1} and 124.53 mV dec^{-1}) and PC electrode (54.9 mV dec^{-1} and 111.38 mV dec^{-1}). This suggests the fastest electron transfer rate of PC-CeO_2 during the redox process of LiPSs. To verify the catalytic capabilities of the different electrodes in facilitating LiPS conversion, symmetric cells were assembled. Fig. 3d shows that the PC-CeO_2 electrode demonstrates the highest current density and the largest curve area, underscoring its excellent catalytic activity in the conversion of LiPSs. In addition, galvanostatic intermittent titration technique (GITT) profiles were measured at 0.1C to explore the

 This journal is © The Royal Society of Chemistry 2025

Open Access Article. Published on 01 December 2025. Downloaded on 1/22/2026 2:28:10 AM.
This article is licensed under a Creative Commons Attribution 3.0 Unported Licence.

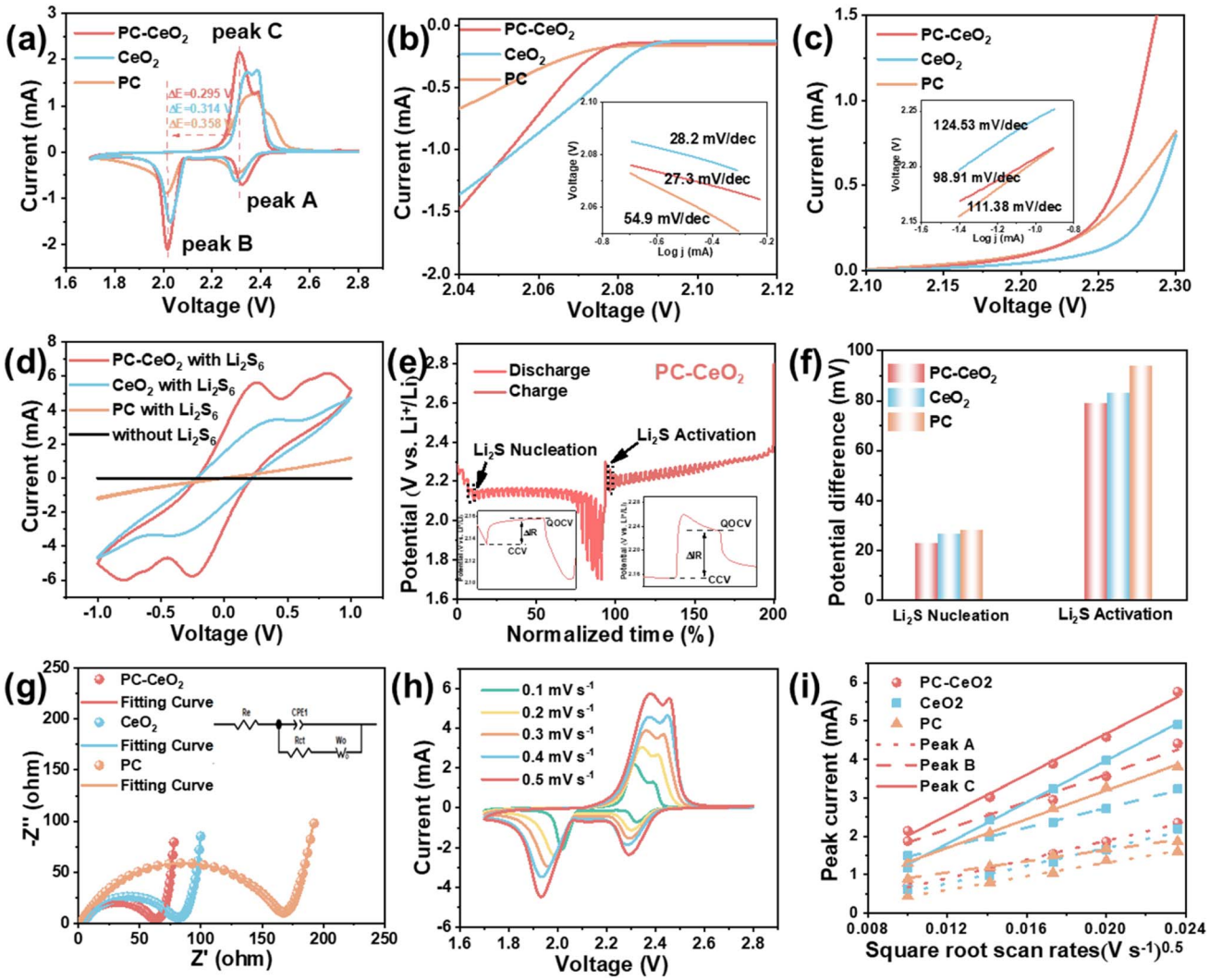

Fig. 3 Electrochemical performances of the PC-CeO_2, CeO_2 and PC electrodes: (a) CV curves at 0.1 mV s^{-1}. (b and c) The relevant section of the CV curves (peaks A and C) and the Tafel plots (Insets). (d) CV curves of the symmetric cells with different electrodes. (e) GITT curve of the PC-CeO_2 electrode. (f) The potential difference at Li_2S nucleation and Li_2S activation point. (g) EIS spectrum. (h) CV profiles of the PC-CeO_2 electrode from 0.1 to 0.5 mV s^{-1}. (i) The corresponding linear fitting of the peak current.

kinetic performance of the host materials (Fig. 3e and S9a–f). Two important transition points about Li_2S nucleation and activation are shown in Fig. 3e, and the voltage difference at Li_2S nucleation and Li_2S activation points can be calculated (Fig. 3f). The cell with the PC-CeO_2 electrode shows the lowest Li_2S nucleation voltage difference (22.8 mV) and Li_2S activation voltage difference (79.1 mV), indicating its lower polarization and faster kinetics. An EIS test was conducted to analyze the redox kinetics (Fig. 3g). The resulting Nyquist plots are presented in Fig. 3g. Notably, the PC-CeO_2 cathode exhibits a relatively low interface resistance (R_s) of 2.72 Ω, compared to 4.74 Ω for the CeO_2 cathode and 2.78 Ω for the PC cathode. Additionally, the PC-CeO_2 cathode displays a relatively small charge transfer resistance (R_{ct}) of 63.9 Ω, in contrast to 81.5 Ω for the CeO_2 and a significantly high value of 167.5 Ω for the PC cathode (shown in Table S2). These results indicate that PC-CeO_2 facilitates the rapid kinetics conversion of LiPSs in Li–S batteries. Furthermore, the CV curves of Li–S cells with different cathodes were recorded over a scan range of 0.1–0.5 mV s^{-1} (Fig. 3h, S10a and S10b). The CV tests were conducted 15 times from 0.1 to 0.5 mV s^{-1}, and the CV curves at the same scanning speed are very close, as depicted in Fig. S11, demonstrating the exceptional electrochemical stability and reversibility of the PC-CeO_2 electrode. The peak current is plotted against the square root of the scan rate, as shown in Fig. 4i. According to the classical Randles–Sevcik equation ($I_P = 2.69 \times 10^5 n^{1.5} A D_{Li^+}{}^{0.5} C_{Li^+} \nu^{0.5}$), the Li^+ diffusion coefficients are calculated. For the PC-CeO_2 electrode, the Li^+ diffusion rates are found to be D_{Li^+} (A) = 2.35×10^{-8} cm^2 s^{-1}, D_{Li^+} (B) = 4.9×10^{-8} cm^2 s^{-1} and D_{Li^+} (C) = 5.21×10^{-8} cm^2 s^{-1}, which are higher than those of the CeO_2 and PC electrodes (Fig. S12). These results demonstrate that the PC-CeO_2 electrode delivers the highest Li^+ diffusion coefficients, leading to faster

Open Access Article. Published on 01 December 2025. Downloaded on 1/22/2026 2:28:10 AM.
This article is licensed under a Creative Commons Attribution 3.0 Unported Licence.

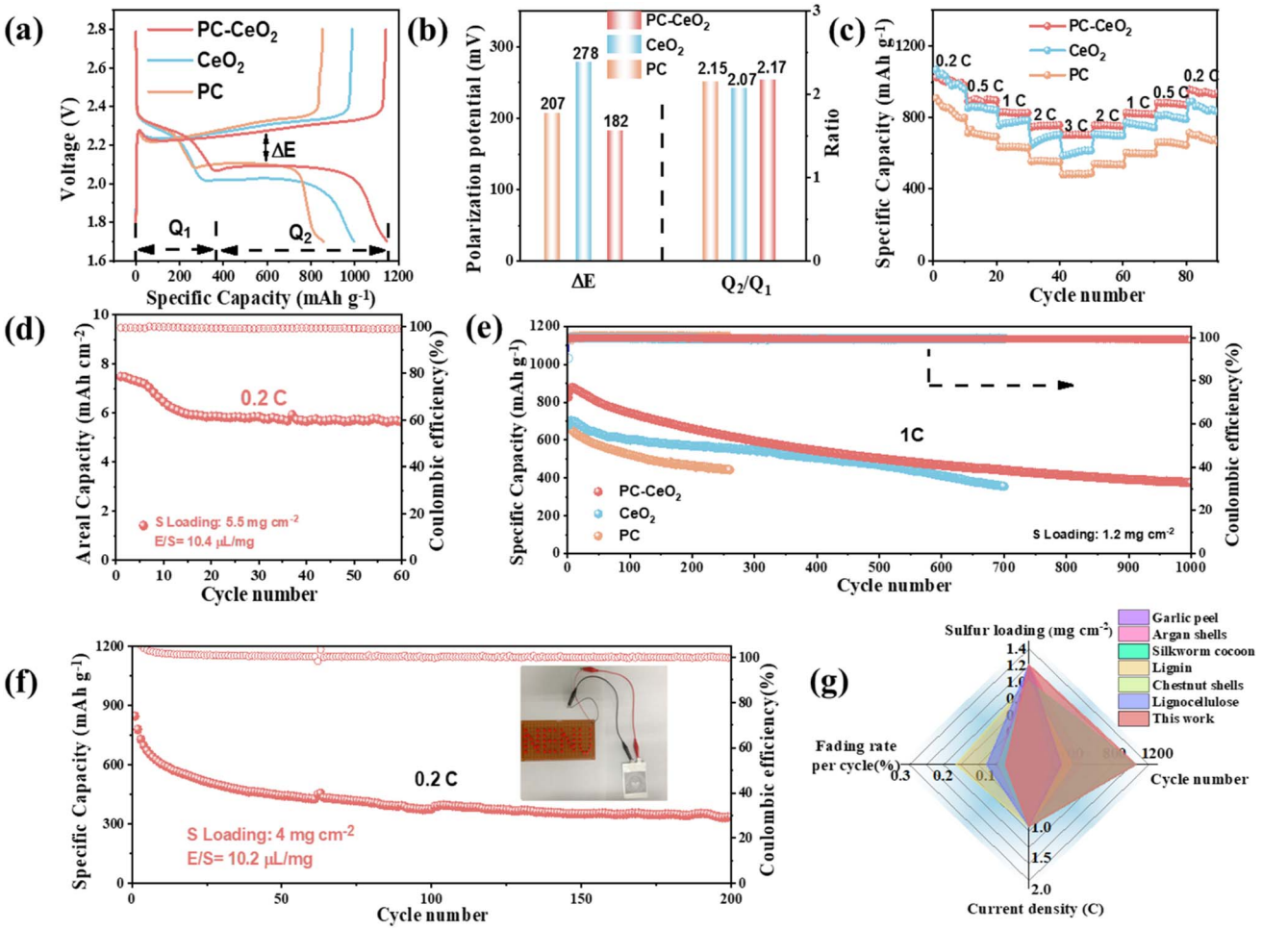

Fig. 4 Electrochemical performances of the PC-CeO_2, CeO_2 and PC electrodes: (a) charging/discharging profiles for the initial cycle at 0.2C. (b) ΔE and Q_2/Q_1 values obtained from discharge/charge curves. (c) rate capability at 0.2–3 C. (d) cycling stability of the PC-CeO_2 electrode at 0.2C with a sulfur loading of 5.5 mg cm^{-2}. (e) Cycling performance at 1C. (f) Cycling performance of the pouch cell assembled with the PC-CeO_2 electrode at 0.2C. (g) Electrochemical performances of different biomass materials.

electrochemical reactions and enhanced performance in Li–S batteries.

Li–S batteries were assembled using PC-CeO_2, CeO_2 and PC electrodes paired with Li anodes. The electrochemical results are summarized in Fig. 4. The charge/discharge profiles show two distinct discharge plateaus and one charge plateau at 0.2C (Fig. 4a), consistent with the CV curve data. Besides, the PC-CeO_2 electrode exhibits a smaller polarization potential (ΔE = 182 mV) than the CeO_2 electrode (ΔE = 278 mV) and PC electrode (ΔE = 207 mV), revealing its enhanced redox kinetics and reversibility in Li–S batteries (Fig. 4b). Moreover, the capacity ratio between the two discharge plateaus (Q_2 and Q_1) serves as a crucial indicator of catalytic activity. Q_1 corresponds to sulfur reduction to soluble LiPSs, while Q_2 reflects their conversion into Li_2S. The PC-CeO_2 electrode shows the highest Q_2/Q_1 ratio of 2.17 (*vs.* 2.07 for CeO_2 and 2.15 for PC), suggesting more efficient sulfur utilization and superior catalytic activity. The cycling performance of the electrodes at 0.2C is depicted in Fig. S13, where the PC-CeO_2 cathode displays an initial discharge capacity of 1174 mAh g^{-1}, with a coulombic efficiency (CE) consistently above 99.8% over 200 cycles, surpassing both the CeO_2 and PC cathodes.

As shown in Fig. 4c, the rate capabilities were further evaluated from 0.2 to 3C. The PC-CeO_2 electrode demonstrates a remarkable rate performance, maintaining initial discharge capacities of 1024.4, 891.5, 829.1, 744.8, and 703.3 mAh g^{-1} at 0.2, 0.5, 1, 2, and 3C, respectively. Even when the current density is reversed back to lower rates (2, 1, 0.5, and 0.2C), the discharge capacities remain at 756.8, 827.3, 883.2, and 957.8 mAh g^{-1}, achieving capacity retention rates of 101.6% at 2C, 99.7% at 1C, 99.1% at 0.5C, and 93.5% at 0.2C, respectively. The corresponding galvanostatic discharge/charge voltage curves of PC-CeO_2, CeO_2 and PC at 0.2–3 C are presented in Fig. S14a–c. The PC-CeO_2 electrode maintains a stable discharge/charge voltage plateau at 3C owing to its enhanced ionic/electronic conductivity, which accelerates the redox reactions of LiPSs. Besides, the PC-CeO_2 cathode delivers an impressive initial specific areal capacity of 7.5 mAh cm^{-2} and maintains a reversible capacity of 5.6 mAh cm^{-2} after 60 cycles at 0.2C at a sulfur loading of 5.5 mg cm^{-2} (Fig. 4d). The long-term cycling stability was tested

 This journal is © The Royal Society of Chemistry 2025

Open Access Article. Published on 01 December 2025. Downloaded on 1/22/2026 2:28:10 AM.
This article is licensed under a Creative Commons Attribution 3.0 Unported Licence.

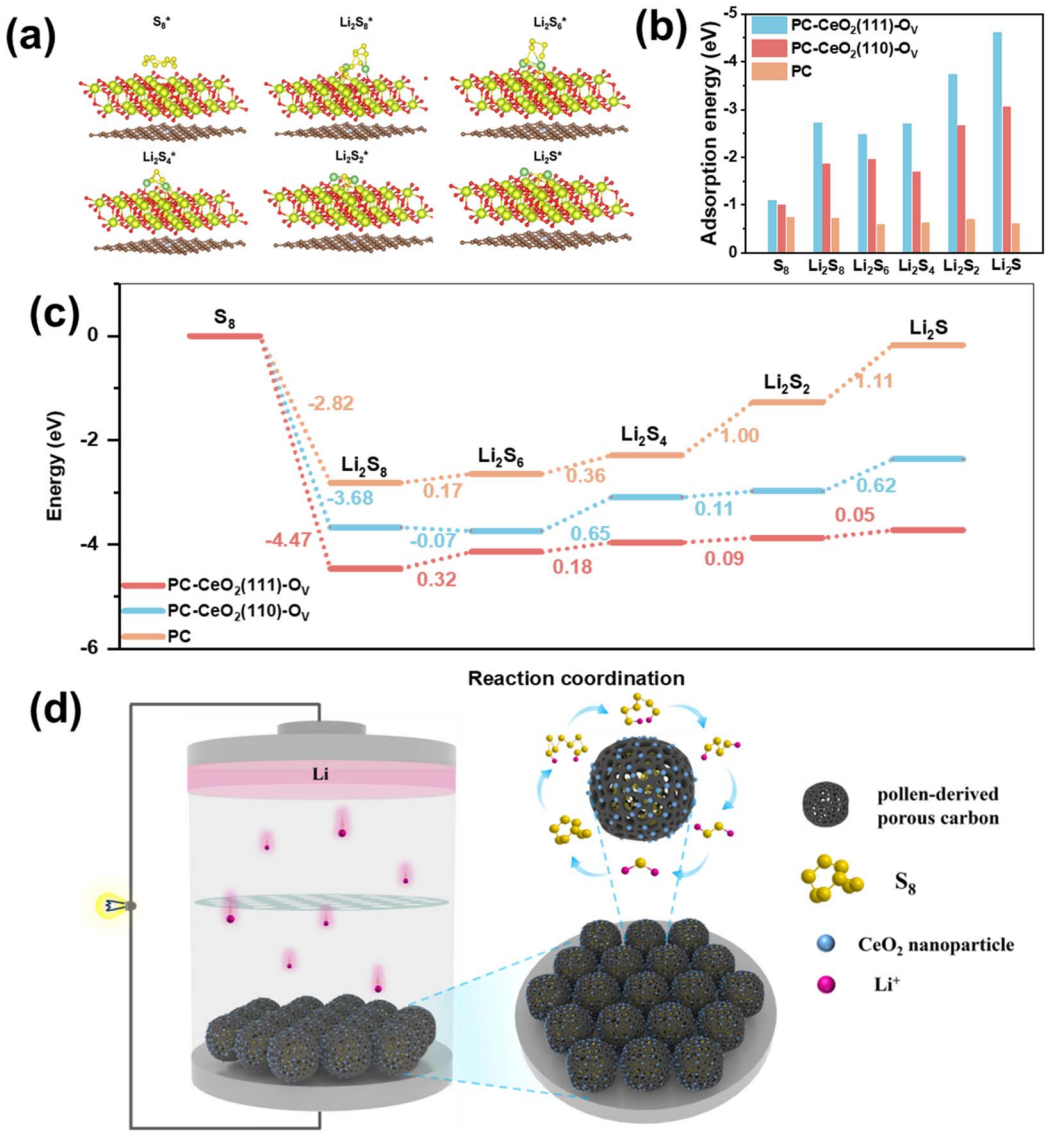

Fig. 5 (a) The corresponding model models of sulfur and LiPSs on the CeO_2 (111) plane. (b) The adsorption energies of sulfur species on the PC-CeO_2 (111), PC-CeO_2 (110) and PC planes. (c) The Gibbs free energies from S_8 to Li_2S on the PC-CeO_2 (111), PC-CeO_2 (110) and PC planes. (d) The mechanism of the PC-CeO_2/S cathode to promote the LiPS conversion.

at 1C (Fig. 4g), where the PC-CeO_2 cathode achieved an initial discharge capacity of 826.2 mAh g^{-1}, gradually declining to 375.1 mAh g^{-1} after 1000 cycles, with an exceptionally low capacity decay rate of just 0.054% per cycle and 0.035% per cycle at 2C, as depicted in Fig. S15. This demonstrates the remarkable cycling stability of the PC-CeO_2 cathode. A pouch cell was constructed to assess the practical viability of the PC-CeO_2 electrode. As displayed in Fig. 4f, the battery exhibits an impressive initial specific capacity of 845.2 mAh g^{-1} at 0.2C. Furthermore, as demonstrated in Fig. S16, a rigorous test of the pouch battery's mechanical properties was conducted by folding it at various angles. Despite these deformations, the battery effortlessly illuminates a "NENU" panel, showing its remarkable anti-folding characteristics and mechanical durability. This underscores the potential of Li–S batteries with PC-CeO_2 cathode for flexible and reliable energy storage applications. In order to further verify the influence of different host materials in Li–S batteries, the cells with the PC-CeO_2 and PC electrodes are disassembled after 500 cycles at 2C, and the SEM images are shown in Fig. S17. First, the SEM images of the sulfur cathodes paired with the PC-CeO_2 and PC electrodes are shown in Fig. S17a and b, respectively. Compared with the cathode assembled with the PC-CeO_2 electrode, the cathode with the PC electrode is severely split after 500 cycles. Besides, the SEM images of Li anodes show that the lithium electrode assembled with the PC-CeO_2 electrode is well protected with a smooth surface and uniform deposition (Fig. S17c). On the contrary, the surface of the lithium electrode with the PC electrode is severely damaged after 500 cycles (Fig. S17d). As illustrated in Fig. S18, the EDS mapping on the cycled separator (a) and cathode (b) shows the uniform distribution of Ce, S, O and N elements. Apart from that, in the XRD patterns of PC-CeO_2 cathode

Open Access Article. Published on 01 December 2025. Downloaded on 1/22/2026 2:28:10 AM. This article is licensed under a Creative Commons Attribution 3.0 Unported Licence.

(Fig. S19), the diffraction peak at 27° is indexed to the (111) planes of Li_2S (PDF#26-1188), which emphasizes the accumulation of Li_2S. In conclusion, the cells with the PC-CeO_2 host material can not only inhibit the shuttle of LiPSs but also adsorb LiPSs and catalyze the conversion. Meanwhile, as illustrated in Fig. 4g and Tables S3 and 4, the electrochemical performance of PC-CeO_2 is more competitive than other sulfur host materials in Li–S batteries.[45–50]

To further explain the adsorption and catalytic capacity of LiPSs for the PC-CeO_2, the density functional theoretical calculations were conducted, and the (111) plane and (110) planes of CeO_2 were chosen as the calculation plane owing to the HRTEM image and the XRD results of PC-CeO_2. The corresponding results are presented in Fig. 5a–c. The adsorption models of sulfur species on PC-CeO_2(111), PC-CeO_2(110) and PC are shown in Fig. 5a, S20 and S21, respectively. As shown in Fig. 5b, PC-CeO_2(111) exhibits the highest adsorption energy towards different sulfur species compared with the PC, and the adsorption energies among Li_2S, Li_2S_2, Li_2S_4, Li_2S_6, Li_2S_8, S_8 and PC-CeO_2 are calculated as −4.61, −3.73, −2.71, −2.48, −2.73 and −1.10 eV, respectively. The above results further illustrate the strong adsorption capacity between PC-CeO_2(111) and LiPSs. Fig. 5c depicts the Gibbs free energy curves for the reduction of sulfur from S_8 to Li_2S on PC-CeO_2(111), PC-CeO_2(110) and PC. The process from S_8 to Li_2S_8 for PC-CeO_2(111), PC-CeO_2(110) and PC is calculated as −4.47, −3.68 and −2.82 eV, respectively, showing that the step is a spontaneous reaction, and the results further show that the process from S_8 to Li_2S_8 for PC-CeO_2(111) is the easiest to proceed. Besides, the highest positive Gibbs free energy (ΔG) in the entire sulfur reduction process is the conversion from Li_2S_2 to Li_2S, marking it the rate-limiting step in the LiPS reduction reaction. Notably, the ΔG for PC-CeO_2(111) is only 0.05 eV, which is lower than 0.62 eV for PC-CeO_2(110) and 1.11 eV for PC, indicating that the PC-CeO_2(111) can accelerate the electrochemical redox reactions of sulfur. Finally, the mechanism of the PC-CeO_2/S cathode to enhance reaction kinetics in Li–S batteries is illustrated in Fig. 5d. On the one hand, the 3D porous structure offers ample space for the loading of CeO_2 NPs as active sites, further offering enough chemisorption sites for LiPSs. On the other hand, the CeO_2 shows remarkable adsorption and catalysis ability to LiPSs, improving the cycle stability and electrochemical performance of the batteries significantly.

3. Conclusion

In summary, the electron-delocalized CeO_2 nanoparticles were anchored on the surface of pollen-derived carbon and acted as host materials for lithium–sulfur batteries. Specifically, the PC-CeO_2 as the sulfur host highlights the following advantages. First, the pollen-derived porous carbon skeleton as the main body of the host accelerates the transfer of electrons and ions, alleviates volume expansion and maintains the structural stability of the sulfur cathode. Second, the introduction and modification of CeO_2 increase the electron delocalization to enhance the chemical adsorption of LiPSs, effectively inhibiting the shuttle of LiPSs and catalyzing its reaction process. Third, owing to the intrinsic structure and properties of these two components, PC-CeO_2 can foster a profound synergistic interaction while maintaining the stability of the overall structure. Finally, the PC-CeO_2/S cathode displays exceptional electrochemical performance, which exhibits a capacity decay rate of 0.054% at 1C after 1000 cycles and an outstanding rate performance of 703.3 mAh g^{-1}at 3C, as well as an excellent high capacity of 5.64 mAh cm^{-2} at 0.2C. This study provides a feasible strategy for the development of biomass and its composites as sulfur hosts in lithium–sulfur batteries.

Conflicts of interest

The authors declare no conflict of interest.

Data availability

The data supporting this article are included in the supplementary information (SI). Supplementary information: experimental section, additional Fig. S1–S21 and Tables S1–4 can be found in supporting information.). See DOI: https://doi.org/10.1039/d5ta08719h.

Acknowledgements

This work is financially supported by the Jilin Provincial Science and Technology Development Foundation (Grant No. 20250102063JC), the Natural Science Foundation of Jiangsu Province (BK 20210130), and the Opening funding from Key Laboratory of Engineering Dielectrics and Its Application (Harbin University of Science and Technology) (No. KFM202507, Ministry of Education) as well as Open Project of Inner Mongolia Engineering Research Center of Lithium–Sulfur Battery Energy Storage (No. MDK2025071). Jian Wang acknowledges the funding provided by the Alexander von Humboldt Foundation. The High-Performance Computing Center of Xiamen University is acknowledged for its supercomputer resources.

References

1 X. Li, Q. Guan, Z. Zhuang, Y. Zhang, Y. Lin, J. Wang, C. Shen, H. Lin, Y. Wang, L. Zhan and L. Ling, *ACS Nano*, 2023, **17**, 1653–1662.
2 J. Wang, J. Zhang, Y. Zhang, H. Li, P. Chen, C. You, M. Liu, H. Lin and S. Passerini, *Adv. Mater.*, 2024, **36**, 2402792.
3 J. Wang, J. Zhang, J. Wu, M. Huang, L. Jia, L. Li, Y. Zhang, H. Hu, F. Liu, Q. Guan, M. Liu, H. Adenusi, H. Lin and S. Passerini, *Adv. Mater.*, 2023, **35**, e2302828.
4 H. Ma, Z. Yu, H. Li, D. Guo, Z. Zhou, H. Jin, L. Wu, X. a. Chen and S. Wang, *Adv. Funct. Mater.*, 2024, **34**, 2310301.
5 F. Zhou, Y. Meng, T. Wang, D. Sun, L. Gao, Z. Sun, Y. Wang, J. Zeng, B. Wang, R. Zhang, R. Li, C. Huang, L. Yang and X. Wang, *Nano Energy*, 2024, **127**, 109755.
6 J. Zhang, C. You, H. Lin and J. Wang, *Energy Environ. Mater.*, 2022, **5**, 731–750.

 This journal is © The Royal Society of Chemistry 2025

Open Access Article. Published on 01 December 2025. Downloaded on 1/22/2026 2:28:10 AM. This article is licensed under a Creative Commons Attribution 3.0 Unported Licence.

7 L. Li, H. Tu, J. Wang, M. Wang, W. Li, X. Li, F. Ye, Q. Guan, F. Zhu, Y. Zhang, Y. Hu, C. Yan, H. Lin and M. Liu, *Adv. Funct. Mater.*, 2023, **33**, 2212499.
8 X. Zhang, X. Li, Y. Zhang, X. Li, Q. Guan, J. Wang, Z. Zhuang, Q. Zhuang, X. Cheng, H. Liu, J. Zhang, C. Shen, H. Lin, Y. Wang, L. Zhan and L. Ling, *Adv. Funct. Mater.*, 2023, **33**, 2302624.
9 J. Wang, J. Zhang, S. Duan, L. Jia, Q. Xiao, H. Liu, H. Hu, S. Cheng, Z. Zhang, L. Li, W. Duan, Y. Zhang and H. Lin, *Nano Lett.*, 2022, **22**, 8008–8017.
10 Z. Yang, Z. Hu, G. Yan, M. Li, Y. Feng, X. Qu and X. Zhang, *J. Colloid Interface Sci.*, 2023, **629**, 65–75.
11 L. Yoshida, T. Hakari, Y. Matsui, M. Deguchi, H. Yamamoto, M. Inoue and M. Ishikawa, *J. Power Sources*, 2024, **624**, 235572.
12 M. Wang, Z. Bai, T. Yang, C. Nie, X. Xu, Y. Wang, J. Yang, S. Dou and N. Wang, *Adv. Energy Mater.*, 2022, **12**, 2201585.
13 H. Li, H. Yang and X. Ai, *Adv. Mater.*, 2023, 2305038.
14 J. Zhang, R. He, Q. Zhuang, X. Ma, C. You, Q. Hao, L. Li, S. Cheng, L. Lei, B. Deng, X. Li, H. Lin and J. Wang, *Adv. Sci.*, 2022, **9**, e2202244.
15 J. Wang, L. Jia, H. Liu, C. Wang, J. Zhong, Q. Xiao, J. Yang, S. Duan, K. Feng, N. Liu, W. Duan, H. Lin and Y. Zhang, *ACS Appl. Mater. Interfaces*, 2020, **12**, 12727–12735.
16 L. Jia, J. Wang, Z. Chen, Y. Su, W. Zhao, D. Wang, Y. Wei, K. Jiang, J. Wang, Y. Wu, J. Li, W. Duan, S. Fan and Y. Zhang, *Nano Res.*, 2019, **12**, 1105–1113.
17 J. Wang, J. Zhang, S. Duan, T. Li, L. Jia, H. Liu, L. Li, S. Cheng, H. Hu, M. Huang, H. Hu, S. Zhang, Q. Xiao and H. Lin, *Chem. Eng. J.*, 2022, **429**, 132352.
18 T. Yang, J. Xia, Z. Piao, L. Yang, S. Zhang, Y. Xing and G. Zhou, *ACS Nano*, 2021, **15**, 13901–13923.
19 D.-S. Kim, S.-G. Woo, C.-J. Kang, J.-H. Lee, J.-N. Lee, J.-S. Yu and Y.-J. Kim, *ChemSusChem*, 2023, **16**, e202202009.
20 M. Zheng, Y. Chi, Q. Hu, H. Tang, X. Jiang, L. Zhang, S. Zhang, H. Pang and Q. Xu, *J. Mater. Chem. A*, 2019, **7**, 17204–17241.
21 B.-J. Lee, T.-H. Kang, H.-Y. Lee, J. S. Samdani, Y. Jung, C. Zhang, Z. Yu, G.-L. Xu, L. Cheng, S. Byun, Y. M. Lee, K. Amine and J.-S. Yu, *Adv. Energy Mater.*, 2020, **10**, 1903934.
22 H. Wang, W. Zhang, J. Xu and Z. Guo, *Adv. Funct. Mater.*, 2018, **28**, 1707520.
23 J. Wang, L. Jia, J. Zhong, Q. Xiao, C. Wang, K. Zang, H. Liu, H. Zheng, J. Luo, J. Yang, H. Fan, W. Duan, Y. Wu, H. Lin and Y. Zhang, *Energy Storage Mater.*, 2019, **18**, 246–252.
24 L. Wang, X. Meng, X. Wang and M. Zhen, *Small*, 2023, **19**, 2300089.
25 P. Chen, T. Wang, D. He, T. Shi, M. Chen, K. Fang, H. Lin, J. Wang, C. Wang and H. Pang, *Angew. Chem., Int. Ed.*, 2023, **62**, e202311693.
26 J. Zhang, C. You, H. Lin and J. Wang, *Energy Ennviron. Mater*, 2022, **5**, 731–750.
27 J. Wang, J. Zhang, S. Cheng, J. Yang, Y. Xi, X. Hou, Q. Xiao and H. Lin, *Nano Lett.*, 2021, **21**, 3245–3253.
28 X. Ren, Q. Wang, Y. Pu, Q. Sun, W. Sun and L. Lu, *Adv. Mater.*, 2023, **35**, 2304120.
29 J. Cho, S. Ryu, Y. J. Gong, S. Pyo, H. Yun, H. Kim, J. Lee, J. Yoo and Y. S. Kim, *Chem. Eng. J.*, 2022, **439**, 135568.
30 K. Zou, W. Jing, X. Dai, X. Chen, M. Shi, Z. Yao, T. Zhu, J. Sun, Y. Chen, Y. Liu and Y. Liu, *Small*, 2022, **18**, 2107380.
31 X. Wang, G. Li, M. Li, R. Liu, H. Li, T. Li, M. Sun, Y. Deng, M. Feng and Z. Chen, *J. Energy Chemistry*, 2021, **53**, 234–240.
32 J. Luo, K. Guan, W. Lei, S. Zhang, Q. Jia and H. Zhang, *J. Energy Chem.*, 2022, **122**, 101–120.
33 Z. Yang, X. Liang, K. Chen, G. Zhang and S. Xing, *J. Energy Storage*, 2024, **102**, 114218.
34 J. Wang, L. Jia, S. Duan, H. Liu, Q. Xiao, T. Li, H. Fan, K. Feng, J. Yang, Q. Wang, M. Liu, J. Zhong, W. Duan, H. Lin and Y. Zhang, *Energy Storage Mater.*, 2020, **28**, 375–382.
35 H. Hu, L. Cui, W. Gao, Z. Zhang and S. Kang, *Chem. Eng. J.*, 2023, **453**, 139516.
36 Q. Xiao, G. Li, M. Li, R. Liu, H. Li, P. Ren, Y. Dong, M. Feng and Z. Chen, *J. Energy Chem.*, 2020, **44**, 61–67.
37 G. Wen, X. Zhang, Z. Shi, Y. Sui, J. Li, J. Zeng, J. Zheng and L. Wu, *J. Colloid Interface Sci.*, 2022, **619**, 106–115.
38 J. Dong, X. Cheng, H. Yang, H. Li, H. Liu, L. Jia, Y. Zhang, Q. Guan, J. Jia, F. Wu, J. Zhang, M. Liu, H. Lin and J. Wang, *Adv. Mater.*, 2025, e2501079, DOI: 10.1002/adma.202501079.
39 J. Zhang, Q. Rao, B. Jin, J. Lu, Q.-g. He, Y. Hou, Z. Li, X. Zhan, F. Chen and Q. Zhang, *Chem. Eng. J.*, 2020, **388**, 124120.
40 G. Wen, Z. Shi, Y. Sui, B. Wang, X. Zhang, Z. Zhang and L. Wu, *J. Colloid Interface Sci.*, 2022, **623**, 697–702.
41 N. P. d. A. Mendes, A. L. d. Souto Neto, J. d. S. Hortêncio, A. L. Menezes de Oliveira, R. A. Raimundo, D. A. Macedo and F. F. da Silva, *ACS Omega*, 2024, **9**, 49913–49924.
42 K. Zou, X. Chen, W. Jing, X. Dai, P. Wang, Y. Liu, R. Qiao, M. Shi, Y. Chen, J. Sun and Y. Liu, *Energy Storage Mater.*, 2022, **48**, 133–144.
43 Y. Song, H. Li, J. Li, J. An, J.-J. Shao and G. Zhou, *J. Energy Chem.*, 2023, **87**, 51–60.
44 H. Jia, J. Fan, P. Su, T. Guo and M.-C. Liu, *Small*, 2024, **20**, 2311343.
45 I. Marri, Z. Edfouf, A. Caballero and A. Y. Tesio, *J. Energy Storage*, 2024, **82**, 110518.
46 X. Wang, M. Niu, C. Gao, Y. Li, T. Li and B. Ren, *Carbon Lett.*, 2024, **34**, 1385–1398.
47 J. Xu, P. Zhou, L. Dai, Y. Gui, L. Yuan, X. Shen, C. Zhang and K. Huo, *Green Chem.*, 2021, **23**, 6008–6019.
48 G. Liu, J. Yang, Y. Wang, H. Lin, M. Zheng, H. Hu, H. Dong, X. Liu, Y. Liu and Y. Xiao, *J. Energy Storage*, 2023, **67**, 107466.
49 F. Liu, P. Feng, M. Yuan, G. Zhai, M. T. Innocent, H. Xiang, Q. Wu, Y. Lu and M. Zhu, *ACS Sustain. Chem. Eng.*, 2023, **11**, 16544–16553.
50 S.-Y. Lee, Y. Choi, J.-K. Kim, S.-J. Lee, J. S. Bae, E. D. Jeong and J. Indus, *J. Ind. Eng. Chem.*, 2021, **94**, 272–281.